A Hybrid String-Inverter/Rectifier Soft-Switched Bidirectional DC/DC Converter

Reza Emamalipour, *Student Member, IEEE*, and John Lam, *Senior Member, IEEE*

***Abstract*—In this article, a new bidirectional dc/dc converter topology based on a hybrid string-inverter/rectifier structure with an isolated *CLLC* resonant circuit is presented for energy storage applications. In this topology, a novel inverter/rectifier leg is presented that enables this circuit to operate in rectifying mode with much lower voltage ripple compared to the standard four-switch string rectifier circuit with the same capacitive filter. Compared to the dual-active-bridge circuit structure, the proposed inverter/rectifier leg is able to reduce the number of high-voltage switches required. A *CLLC* resonant circuit is employed to step-up/down the dc voltage levels. The operating principles of the proposed converter are discussed in this article. Silicon Carbide switches are used in both legs of the proposed converter, with zero-voltage switching turn-ON and zero-current switching (ZCS) turn-OFF realized for all switches, whereas ZCS turn-ON and OFF are achieved for all diodes. Simulation and experimental results are provided on a 1-kW, 100-kHz, 400-V/700-V converter system to highlight the merits of the proposed converter. Experimental results demonstrated that an efficiency of close to 97% is achieved in the proposed converter in both boost mode and buck mode at the full-load condition.**

***Index Terms*—Bidirectional converters, *CLLC* resonant circuit, dc/dc converters, electric vehicle (EV), soft switching.**

I. Introduction

FOR almost a quarter century, conventional energy sources (fossil fuels) have been depleted and are gradually becoming economically nonviable. As a result, renewable energy sources (e.g., wind and solar) and electric vehicles (EVs), are becoming attractive replacements [1], [2]. Recently, EV charging systems have drawn attention in the [3], [4]. A typical unidirectional grid-to-vehicle charger consists of an ac/dc power factor correction stage and a dc/dc converter [5]. Yet, EVs can also be utilized to send either active or reactive power back to the grid to provide voltage and frequency regulation [6].

Bidirectional converters are essential in allowing two-way power flow and are also applied to interface the battery bank with the high-voltage dc-link of the inverter in EV applications [7]. Fig. 1 shows the structure of the integrated charging system for an EV. The high-voltage and low-voltage battery packs are connected to the dc bus by means of bidirectional dc/dc converters. To maintain the bus voltage constant, the bidirectional converter controls the battery charge and discharge and prolongs its service life, and reduces the operation and maintenance costs of the entire power generation system [8].

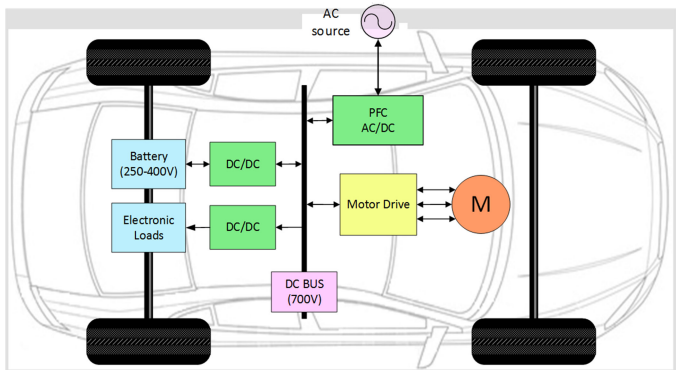

Fig. 1. Structure of the integrated charging system for EV.

Several different types of bidirectional converters have been discussed in [9]–[13]. In low-voltage low-power applications, a two-quadrant nonisolated buck/boost bidirectional converter has been preferred in many studies due to its simple structure, low cost, and high efficiency. However, in medium to high-voltage/-power applications such as the dc/dc bidirectional converter in EVs, the two-switch structure exhibits several shortcomings, including low efficiency at light load [14]. In [15], a bidirectional flyback converter is presented. It is simple and is able to achieve soft-switching operation, but its efficiency suffers at high-power applications.

Dual-active-bridge (DAB)-based dc/dc converters and *CLLC* resonant converters are widely used for providing bidirectional power flow and achieving zero-voltage-switching (ZVS) [16]–[19]. Yet, the conventional DAB converter has high circulating reactive current, its soft-switching region of a conventional DAB converter is only limited to a narrow output voltage range and the voltage stress across each power switch is equal to the dc-link voltage. Compared to DAB-based bidirectional converters, resonant converters have the advantage of achieving soft switching at almost all loading conditions [20]. Different types of resonant bidirectional converters have been reported in [21]–[23].

Three-level (TL)-based bidirectional converters have been reported in the [24]–[29]. They are popular as they are able to reduce the voltage stress across the switches while doubling the

Manuscript received July 30, 2019; revised November 3, 2019; accepted December 17, 2019. Date of publication December 26, 2019; date of current version April 22, 2020. This work was supported in part by the Natural Sciences and Engineering Research Council (NSERC). Recommended for publication by Associate Editor K. Akatsu. *(Corresponding author: John Lam.)*

R. Emamalipour is with the Lassonde School of Engineering, York University, Toronto, ON M3J 1P3, Canada (e-mail: remamali@cse.yorku.ca).

J. Lam is with the Electrical Engineering and Computer Science, York University, Toronto, ON M3J 1P3, Canada (e-mail: johnlam@cse.yorku.ca).

Color versions of one or more of the figures in this article are available online at http://ieeexplore.ieee.org.

Digital Object Identifier 10.1109/TPEL.2019.2962518

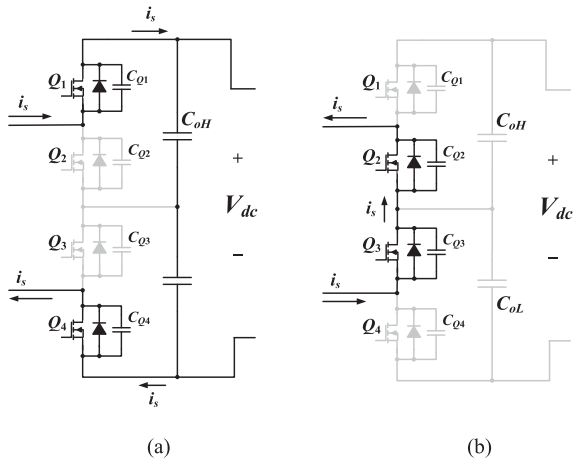

Fig. 2. Topology of the conventional four-switch string converter (operating as a rectifier) including the current path for: (a) positive i_s, and (b) negative i_s.

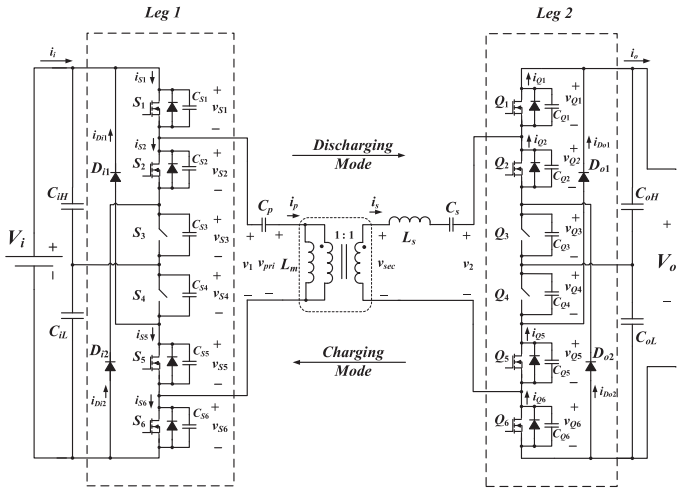

Fig. 3. Proposed hybrid string-inverter/rectifier structured soft-switched bidirectional converter.

frequency of the output voltage ripple when the circuit operates in rectifying mode, hence reducing the output voltage ripple. Due to the asymmetric loss distribution between the inner and outer switches in the TL circuit, and the dc-link capacitor unbalance voltage distribution, active TL circuit has been reported [26] by replacing the two diodes with switches. In [27], a comparative study on various TL-based resonant and soft-switching converters has been reported. A drawback with the TL circuit when it is used in conjunction with resonant circuits is that as the duration of the zero-voltage level increases at the output of the inverter, the maximum achievable gain of the resonant converter decreases. It also loses soft-switching operation as the converter operates away from the full-load condition [27]. Different additional passive or active auxiliary circuits [24], [27], [28] have been reported to aid the TL converter to extend soft-switching operation.

Another type of bidirectional converters for the use in energy storage applications is the four-switch string-structured rectifier/inverter circuit [30], [31] (see Fig. 2) in which the voltage stress equally distributed among the switches and is reduced by half compared to that of the conventional full-bridge inverters, making it a suitable choice for medium- and high-voltage applications [30]. However, in this circuit, when it operates in rectifying mode, the circuit operates as a half-wave rectifier and only the positive current flows through the output capacitor, while the negative current circulates in the resonant circuit, leading to higher voltage ripple in the load with the frequency of the output current ripple equal to the switching frequency [31].

A five-switch H-bridgeless dc/dc bidirectional converter has been presented in [31] that utilizes only one low-frequency (LF) switch and one dc-link capacitor. The main drawback of this converter is that no neutral point is available in the circuit topology. Consequently, in case there is a difference in the values of the snubber capacitors, the input voltage is not equally distributed over the switches. In addition, the switches in the OFF state experience a fluctuating voltage stress. Hence, the voltage across all the switches is not completely balanced.

In this article, a new bidirectional dc/dc converter topology based on a hybrid string-inverter/rectifier structure with an isolated *CLLC* resonant circuit is proposed. The proposed converter resembles the conventional four-switch string topology, while the magnitude of the input/output voltage ripples are able to be reduced compared to that of the conventional four-switch string topology. Compared to the converter presented in [31], the proposed converter provides a neutral point that ensures that the voltage is distributed equally over the switches and any difference in the values of the snubber capacitors does not affect the voltage stress over the switches. A *CLLC* resonant circuit is designed to step up/down the dc voltage levels. In addition, the proposed converter provides soft-switching conditions for all switches and diodes. The same operating frequency can also be used to achieve both step-up/step-down voltage conversions. The operating principles and descriptions of the proposed circuit will be provided. The performance of the proposed bidirectional dc/dc converter is verified through simulation and experimental results on a 1-kW, 400-V/700-V converter system.

This article is organized as follows. Section II provides a description and the operating principles of the proposed bidirectional converter. Section III provides the analysis on achieving soft-switching conditions of the circuit, as well as all the design equations. Section IV provides the loss analysis of the circuit and Section V provides the simulation and experiment results to highlight the merits of this work. Finally, the concluding remarks and discussions are provided in Section V.

II. Proposed Isolated Bidirectional Converter

The proposed bidirectional dc/dc converter is shown in Fig. 3. In the proposed circuit, each inverter or rectifier leg consists of four high-frequency (HF) switches and two LF switches. The two legs, as shown in Fig. 3, are then connected via an isolated *CLLC* resonant circuit. The proposed converter can operate in boost conversion mode (i.e., discharging mode with V_i represents the battery voltage, and V_o represents the dc-bus voltage) or buck conversion mode (i.e., charging mode).

When leg 1 operates as an inverter, the inverter generates a unipolar square wave voltage across the resonant tank. In this case, the two middle LF switches (S_3 and S_4) are ON and the inverter operates as the conventional four-switch string inverter, resulting in a voltage stress of half of the input voltage across each switch. In the rectifying side (i.e., leg 2), the two middle switches (Q_3 and Q_4) are OFF, allowing the output current pass through the output capacitors (C_{OH} and C_{OL}) for both positive and negative currents. As a result, compared to the conventional four-switch string rectifier, the secondary-side rectifier in the proposed circuit acts as a full-wave rectifier and is able to achieve lower output voltage ripple of the converter than that of the conventional four-switch rectifier circuit. On the other hand, when the converter operates in buck mode (i.e., charging mode), the two middle LF switches (Q_3 and Q_4) in leg 2 are ON with the two middle LF switches in leg 1 (S_3 and S_4) turn OFF. In order to step up/down the voltage level and to provide ZVS for the switches during turn-ON and turn-OFF, a *CLLC* resonant circuit is employed in the proposed converter. An integrated HF transformer is utilized in the resonant circuit for offering galvanic isolation between the primary and secondary sides. Therefore, all the semiconductor devices in the proposed circuit achieve either ZVS or ZCS operation.

The proposed converter can also be used in a modular structure. In the modular converter, based on the application, each module can be connected in either parallel/cascaded inputs or parallel/cascaded outputs. A modular converter structure with the proposed circuit modules in parallel is shown in Fig. 4.

The key operating waveforms of a single module are demonstrated in Fig. 5. Since the proposed circuit is bidirectional, only the operating principles of the boost operating mode (i.e., discharging mode) is discussed later.

The detailed operating states of the converter in each time interval have been provided in Fig. 7.

A. Interval 1 [$t_0 < t < t_1$]:

At $t = t_0$, the gate signals are applied to S_1 and S_6, while S_2 and S_5, Q_1–Q_6 are OFF and S_3 and S_4 are ON. The primary-side resonant current (i_p) is negative and the current passes through the body diodes of S_1 and S_6 until it reaches zero. Meanwhile, the secondary-side resonant current (i_s) is positive and the antiparallel diodes of Q_1 and Q_6 conduct the current.

B. Interval 2 [$t_1 \leq t < t_2$]:

In this interval, S_1, S_3, S_4, and S_6 are still ON, while the rest of the switches are OFF. At $t = t_1$, i_p becomes positive and passes through S_1 and S_6. Hence, S_1 and S_6 turn ON under ZVS. At the same time, i_s is still positive passing through the body diodes of Q_1 and Q_6.

C. Interval 3 [$t_2 \leq t < t_3$]:

The gate signals remain unchanged in this interval, yet i_s becomes negative at $t = t_2$. At this point, Q_3 and Q_4 prevent v_2 from being short circuit and allow the negative current to flow through D_{o1} and D_{o2} and the antiparallel diodes of Q_2 and Q_5 charging C_{oH} and C_{oL}.

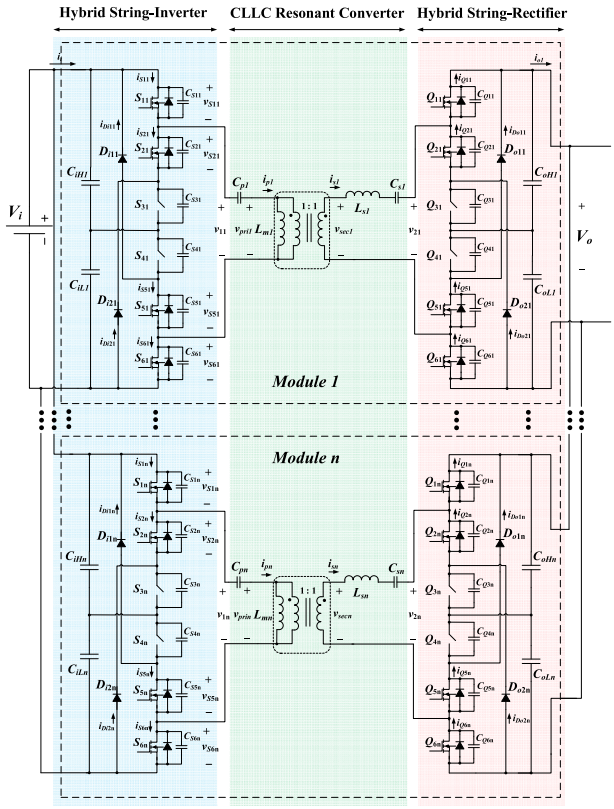

Fig. 4. Modular converter structure with the proposed hybrid string-inverter/rectifier resonant bidirectional dc/dc converter module.

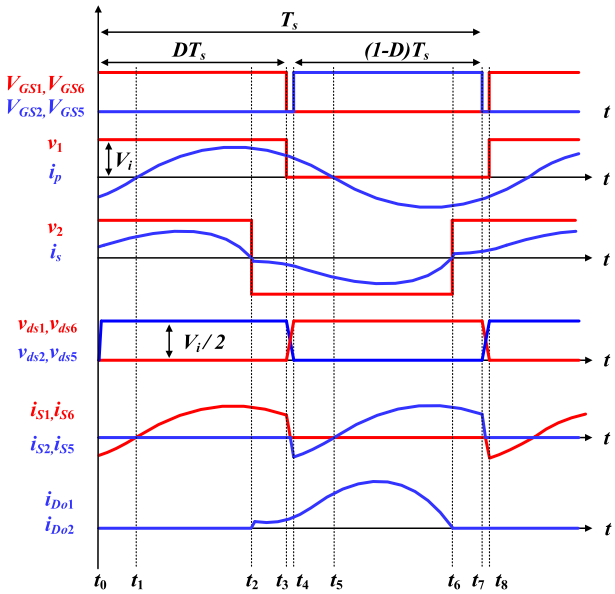

Fig. 5. Key waveforms of the dc/dc portion in the proposed converter.

D. Interval 4 [$t_3 \leq t < t_4$]:

At $t = t_3$, the gate signals of S_1 and S_6 are removed. i_p is positive and flows through C_{S2} and C_{S5} discharging them while

charging C_{S1} and C_{S6}. As a result, v_{S1} and v_{S6} rise slowly from zero, providing ZCS for S_1 and S_6. The flowing path for i_s remains unchanged.

E. Interval 5 [$t_4 \leq t < t_5$]:

At $t = t_4$, the gate signals of S_2 and S_5 are applied while S_1, S_6, Q_1–Q_6 are OFF and S_3 and S_4 are ON. i_p is positive and the current passes through the body diodes of S_2 and S_5 until it reaches zero. i_s is negative and passes through D_{o1} and D_{o2} and the antiparallel diodes of Q_2 and Q_5.

F. Interval 6 [$t_5 \leq t < t_6$]:

In this interval, the gate signals remain unchanged. At $t = t_5$, i_p becomes negative and passes through S_2 and S_5 providing ZVS turn ON. The current path for i_s remains unchanged.

G. Interval 7 [$t_6 \leq t < t_7$]:

S_2 and S_5 are still ON while S_1, S_6, Q_1–Q_6 are turned OFF. i_s becomes positive at $t = t_6$ and passes through the antiparallel diodes of Q_1 and Q_6 charging C_{oH} and C_{oL}.

H. Interval 8 [$t_7 \leq t < t_8$]:

At $t = t_7$, the gate signals of S_2 and S_5 are removed. i_p is negative and flows through C_{S1} and C_{S6} discharging them while charging C_{S2} and C_{S5} making v_{S2} and v_{S5} rise slowly from zero, providing ZCS for S_2 and S_5.

III. Design Consideration and Analysis of Soft-Switching Condition

This section is going to analyze the characteristics of the employed *CLLC* resonant circuit and the converter's soft-switching operating condition. Fundamental harmonic analysis is used to analyze the circuit voltage gain in both boost mode and buck mode. Consider the boost operating mode, as mentioned in the previous section, S_1 and S_6 turn ON during DT_s and operate in complementary fashion with S_2 and S_5 turn ON in interval $(1–D)T_s$, where D is the duty ratio and T_s is the switching period. Unipolar square wave voltage v_1, as given by (1), is generated by the inverter and is applied to the primary of the resonant circuit, where θ_h is given by (2), where h is the harmonic order, $\omega_{\rm sw}$ is the angular switching frequency, and V_i is the input voltage. Since the capacitors in the resonant tank block the dc component, the voltage at the primary side of the resonant circuit (v_1) can be written, as given by (3)

$$v_1 = V_i D + \sum_{h=1}^{\infty} \frac{\sqrt{2}V_i}{h\pi}\sqrt{(1-\cos 2h\pi D)}\sin(h\omega_{sw}t + \theta_h) \tag{1}$$

$$\theta_h = \tan^{-1}\left(\frac{\sin 2h\pi D}{1-\cos 2h\,\pi D}\right) \tag{2}$$

$$v_1 = \sum_{h=1}^{\infty} \frac{\sqrt{2}V_i}{h\pi}\sqrt{(1-\cos 2h\pi D)}\sin(h\omega_{\rm sw}t + \theta_h). \tag{3}$$

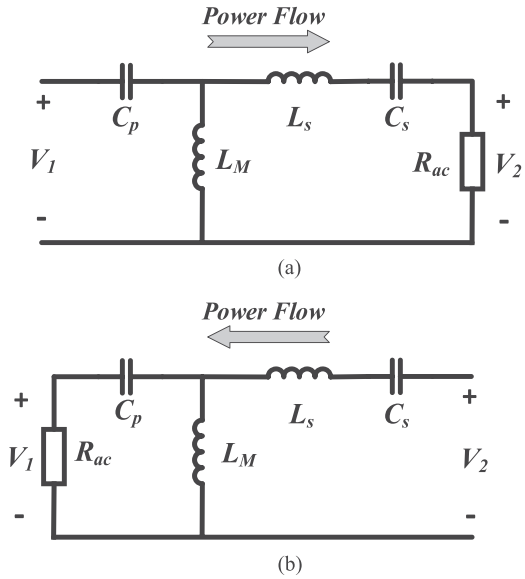

Fig. 6. Fundamental equivalent circuit in (a) boost mode (b) buck mode.

Since the output voltage of the converter is regulated by varying the switching frequency, in order to maximize the voltage at the primary side of the resonant circuit, D is set to 50%. v_1 can then be expressed, as given by (4). By ignoring the higher order harmonics and only considering the fundamental frequency of the voltage at the primary of the resonant circuit, the rms value of v_1 ($V_{1(\rm rms)}$) is given by (5).

$$v_1 = \sum_{h=\rm odd}^{\infty} \frac{2V_i}{h\pi}\sin(h\omega_{\rm sw}t) \tag{4}$$

$$V_{1(\rm rms)} = \frac{\sqrt{2}V_i}{\pi}. \tag{5}$$

Fig. 6 shows the fundamental harmonic equivalent resonant circuit. The *CLLC* resonant tank consists of L_M, L_s, C_p, and C_s, where L_M represents the magnetizing inductance of the HF transformer, C_p and C_s stand for the primary- and secondary-side capacitors, respectively, and L_s represents the secondary-side inductance. In addition, $k = L_s/L_M$ is defined as the ratio between the secondary side and the magnetizing inductances and $m = C_s/C_p$ is the ratio between the secondary-side and the primary-side capacitances. The equivalent resistance $R_{\rm ac}$, as shown in (6), and the angular resonant frequency ω_0 (rad/s) of the resonant components, as given in (8), are chosen as the base values, where N_p and N_s are the number of turns in the primary and secondary of the HF transformer, respectively, and R_L is the output equivalent resistance of the resonant circuit

$$R_{\rm ac} = \frac{8}{\pi^2}\cdot\left(\frac{N_p}{N_s}\right)^2\cdot R_L. \tag{6}$$

Since the turn ratio of the HF transformer is 1, the equivalent ac resistance $R_{\rm ac}$ can be expressed by (7), where ωr is the normalized angular switching frequency and is given by (10)

and Q represents the quality factor

$$R_{\rm ac} = \frac{8}{\pi^2} \cdot R_L \tag{7}$$

$$\omega_0 = \frac{1}{\sqrt{L_M C_p}} \tag{8}$$

$$Q = \frac{R_{\rm ac}}{L_M \cdot \omega_0} = R_{\rm ac} \cdot C_p \cdot \omega_0 \tag{9}$$

$$\omega_r = \frac{\omega_{\rm sw}}{\omega_0}. \tag{10}$$

Considering the aforementioned assumptions and by ignoring the higher order harmonics, the voltage gain in the boost operating mode is given by

$$\frac{V_2}{V_1} = \frac{R_{\rm ac} \cdot jL_M\omega_{\rm sw} \cdot jC_p\omega_{\rm sw}}{\left(R_{\rm ac} + jL_M\omega_{\rm sw} + \frac{1}{jmC_p\omega_{\rm sw}}\right) \cdot jL_M\omega_{\rm sw} \cdot jC_p\omega_{\rm sw} + R_{\rm ac} + j(k+1)L_M\omega_{sw} + \frac{1}{jmC_p\omega_{\rm sw}}}. \tag{11}$$

Using (7)–(10), the voltage gain can be further simplified as

$$\frac{V_2}{V_1} = \frac{{\omega_r}^2}{({\omega_r}^2 - 1) + j\frac{1}{Q}\left(k{\omega_r}^3 - \frac{\omega_r}{m} - k\omega_r + \frac{1}{m\omega_r} - \omega_r\right)}. \tag{12}$$

Using the same method, the voltage gain in the buck operating mode is obtained as given by

$$\frac{V_1}{V_2} = \frac{j\omega_r}{\frac{1}{Q}\left(1 + \frac{1}{m} - \frac{1}{m{\omega_r}^2} + k\left(1 - {\omega_r}^2\right)\right) + j\left(\omega_r - \frac{1}{m\omega_r} + k\omega_r\right)}. \tag{13}$$

As can be seen in Fig. 7, the two middle LF switches (Q_3 and Q_4) and the diodes in the rectifying side allow the current to flow through the output capacitors for both positive and negative secondary-side resonant current (i_s), allowing the rectifying circuit to operate as a full wave rectifier. The gain of the rectifying stage is given by (14).

Hence, the total voltage gain of the proposed converter in the boost operating mode is given by (15), where V_o is the output voltage of the converter and V_2 is the voltage in the secondary side of the resonant circuit

$$\frac{V_o}{V_2} = \frac{\pi}{2\sqrt{2}} \tag{14}$$

$$G_{\rm disch} = \left|\frac{V_o}{V_2} \times \frac{V_2}{V_1} \times \frac{V_1}{V_i}\right| = \frac{{\omega_r}^2}{\sqrt{\left({\omega_r}^2 - 1\right)^2 + \frac{1}{Q^2} \times \left(k{\omega_r}^3 - \frac{\omega_r}{m} - k\omega_r + \frac{1}{m\omega_r} - \omega_r\right)^2}}. \tag{15}$$

Similarly, the total voltage gain of the proposed converter in the buck operating mode is obtained as follows:

$$G_{\rm ch} = \frac{1}{2} \times \frac{\omega_r}{\sqrt{\frac{1}{Q^2}\left(1 + \frac{1}{m} - \frac{1}{m{\omega_r}^2} + k\left(1 - {\omega_r}^2\right)\right)^2 + \left(\omega_r - \frac{1}{m\omega_r} + k\omega_r\right)^2}}. \tag{16}$$

The voltage gain curves of the converter in both boost and buck modes are demonstrated in Figs. 8 and 9, respectively, for $k = 1$ and $m = 1$.

Typically, the battery pack voltage in EVs goes from a minimum value of 250 V to a maximum value of 400 V, with a nominal value of 345 V (e.g., Nissan Leaf). Based on the structure of the integrated charging system shown in Fig. 1, the dc-bus voltage $V_{\rm DC}$ must be higher than the peak magnitude of the line-to-line grid voltage $V_{gg,p}$ of a confidence factor C_f that accounts for the voltage drops across ac filter and the power switches inside the ac/dc block [32]

$$V_{\rm DC} = C_f \cdot V_{gg,p}. \tag{17}$$

By selecting a convenient confidence factor, generally, a dc-bus voltage of 700 V is considered in the design of EVs. Consequently, in order to allow the converter to achieve the required specifications, a quality factor of 4 is selected in the design of the resonant circuit. Furthermore, for a given quality factor, *k* and *m* can be adjusted to make the voltage gain of 700 V to 400 V happen for the same switching frequency in both buck and boost modes. Fig. 10 demonstrates the voltage gain curve of the proposed dc/dc converter for $Q = 4$, $k = 2$, and $m = 0.35$.

From (3), the primary-side resonant current of the converter (i_p) is then obtained (18), where $|Z_{i,h}|$ is the amplitude of the equivalent impedance of the *h*th harmonic and is given by (19), and $\varphi_{\rm Zi,h}$ represents the phase angle given by (20)

$$i_p = \sum_{h=1}^{\infty} \frac{\sqrt{2}V_i}{h\pi\left|Z_{i,h}\right|}\sqrt{(1 - \cos 2h\pi D)}\sin(h\omega_{sw}t + \theta_h - \varphi_{Z_{i,h}}) \tag{18}$$

$$|Z_{i,h}| = R_{\rm ac} \cdot \sqrt{\frac{\left(k + 1 + \frac{1}{m}\left(1 - \frac{1}{h^2\omega_r^2}\right) - k\omega_r^2\right)^2 + \left(hQ\omega_r \cdot \left(1 - \frac{1}{h\omega_r^2}\right)\right)^2}{Q^4 + \left(hQ\omega_r \cdot \left(k + 1 - \frac{1}{mh\omega_r^2}\right)\right)^2}} \tag{19}$$

$$\varphi_{Z_{i,h}} = \tan^{-1}\left(\frac{hQ\omega_r \cdot \left(1 - \frac{1}{h\omega_r^2}\right)}{k + 1 + \frac{1}{m} \cdot \left(1 - \frac{1}{h^2\omega_r^2}\right) - k\omega_r^2}\right) - \tan^{-1}\left(\frac{h\omega_r \cdot \left(k + 1 - \frac{1}{mh\omega_r^2}\right)}{Q}\right). \tag{20}$$

The peak value of the primary resonant current $(I_{p(\max)})$ and the rms value of the fundamental component of the primary resonant current $(I_{p(\rm rms)})$ are then obtained, as shown in (7)

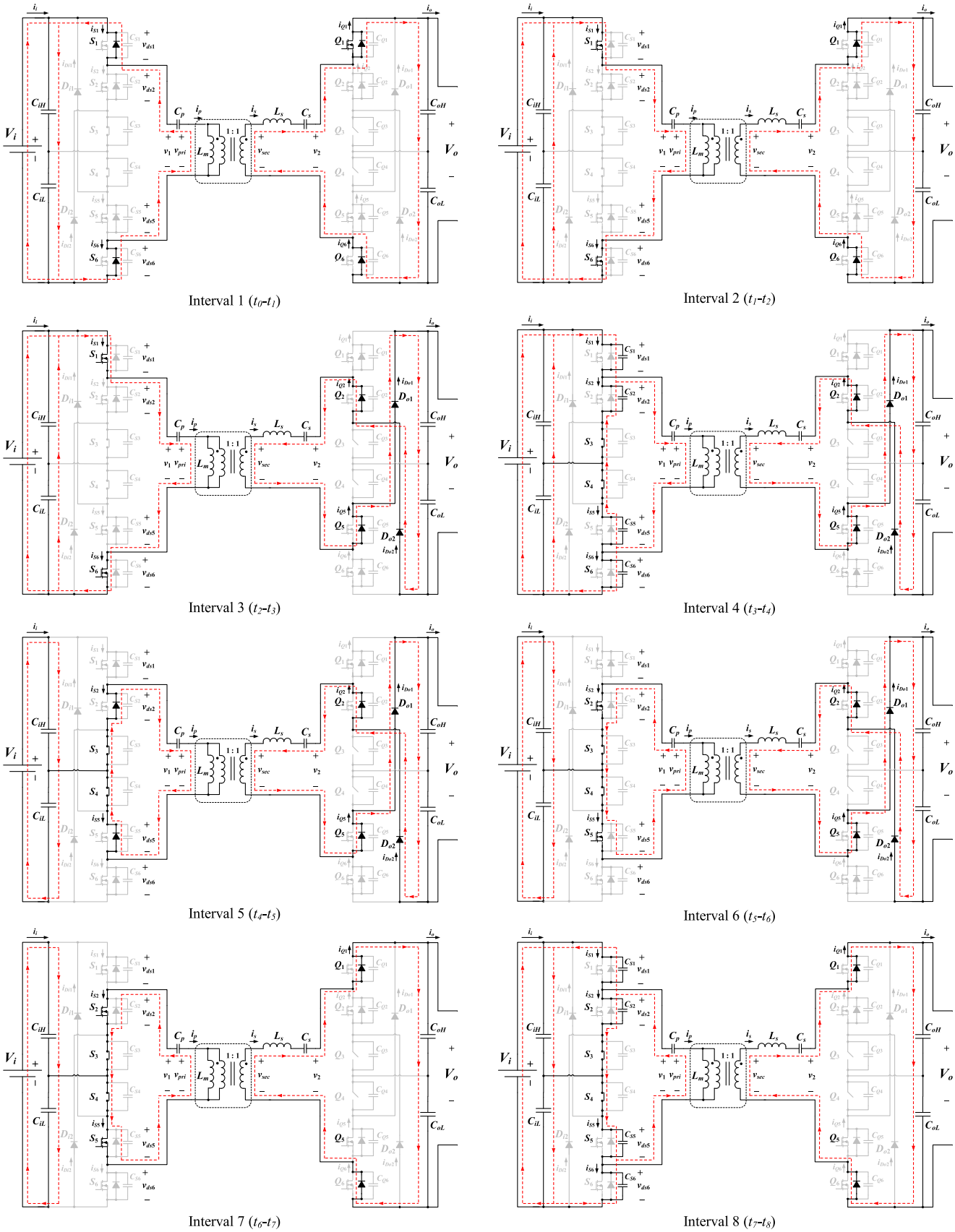

Fig. 7. Operating stages of the proposed converter.

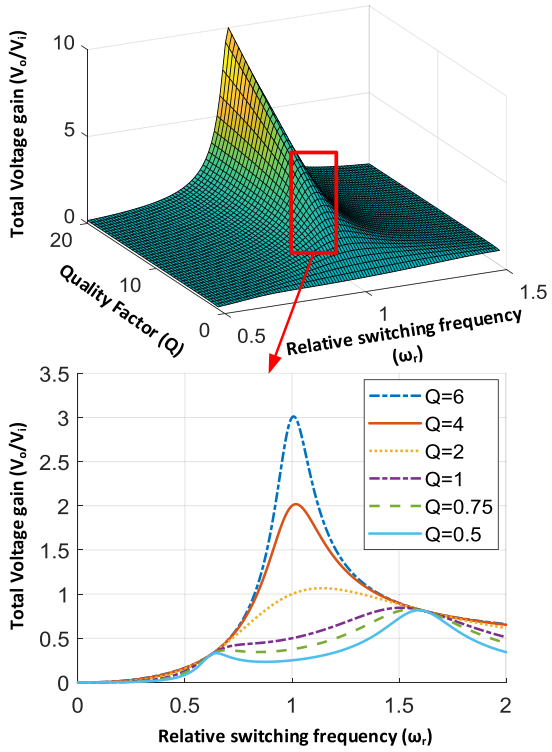

Fig. 8. Voltage gain plot of the proposed converter in boost mode for $k = 1$ and $m = 1$.

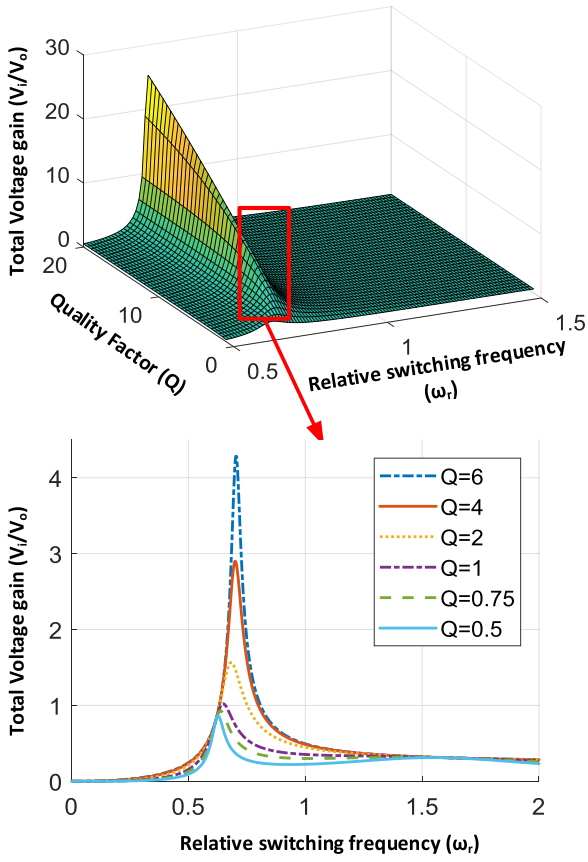

Fig. 9. Voltage gain plot of the proposed converter in buck mode for $k = 1$ and $m = 1$.

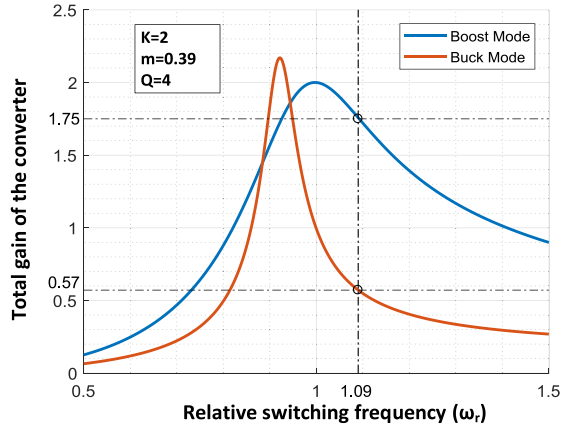

Fig. 10. Voltage gain curves in the proposed converter.

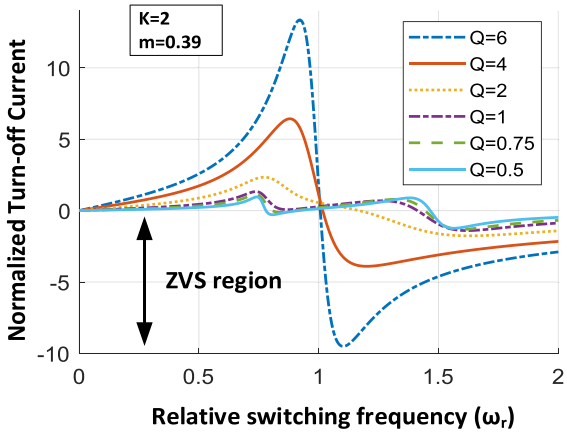

Fig. 11. Normalized rms value of the primary-side resonant current at $t = t_0$ and $d = 0.5$.

and (8), respectively

$$I_{p(\max)} = \sum_{h=1}^{\infty} \frac{\sqrt{2}V_i}{h\pi\,|Z_{i,h}|}\sqrt{(1-\cos 2h\pi D)} \tag{21}$$

$$I_{p(\mathrm{rms})} = \frac{V_i}{\pi}\cdot\sum_{h=1}^{\infty}\sqrt{\frac{1-\cos 2h\pi D}{(h\,|Z_{i,h}|)^2}}. \tag{22}$$

Further, from (18), the per unit fundamental component of the current in the primary of the resonant circuit for $t = t_0$ and $t = t_4$ is obtained in (23) and (24), respectively.

$$i_p(t_0) = \frac{\sqrt{2}}{\pi}\sqrt{(1-\cos 2h\pi D)}\sin(\theta_h - \varphi_{Zi,h}) \tag{23}$$

$$i_p(t_4) = \frac{\sqrt{2}}{\pi}\sqrt{(1-\cos 2h\pi D)}\sin(2\pi hD + \theta_h - \varphi_{Zi,h}). \tag{24}$$

As can be observed from Fig. 5, in order to provide soft switching for S_1 and S_6, i_p has to be negative at $t = t_0$. The curve of i_p for $D = 0.5$ and different values for ω_r and Q is shown in Fig. 11 along with the soft-switching area. Similarly, for S_2 and S_5 to turn ON under ZVS, i_p has to be positive at $t = t_4$. With $D = 0.5$, the soft switching curve for S_2 and S_5 is the same

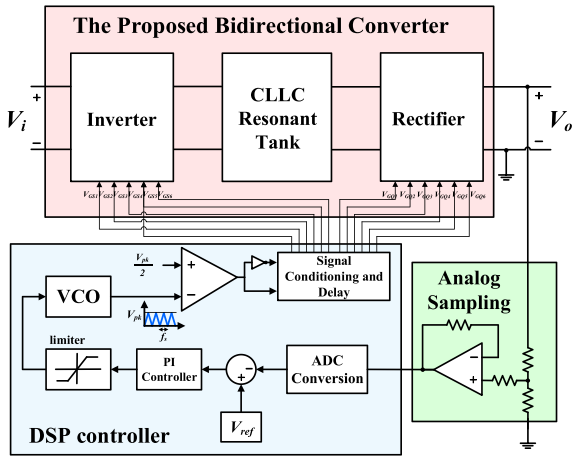

Fig. 12. Block diagram of the closed-loop system.

and the current is mirrored with a negative sign. Considering the aforementioned assumptions and the specified operating point, shown in Fig. 10, soft switching is realized for all of the switches in boost operating mode.

Therefore, for an output power of 1 kW and a base switching frequency of 100 kHz, the resonant circuit components are obtained as

$$R_L = \frac{{V_o}^2}{P_o} = \frac{700^2}{1000} = 490\,\Omega \tag{25}$$

$$R_{\rm ac} = \frac{8}{\pi^2} \cdot R_L = 397.18\,\Omega \tag{26}$$

$$L_M = \frac{R_{\rm ac}}{Q \cdot 2\pi f_0} = 158\ \mu{\rm H} \tag{27}$$

$$L_s = k \cdot L_M = 316.07\ \mu{\rm H} \tag{28}$$

$$C_p = \frac{1}{L_M \omega_0^2} = 16.03\ {\rm nF} \tag{29}$$

$$C_s = mC_p = 6.25\ {\rm nF}. \tag{30}$$

A. Control Principles and Voltage Balancing Technique

The block diagram of the control system is demonstrated in Fig. 12. The output voltage of the converter can be controlled via the variable-frequency method or duty ratio control through the pulsewidth modulation technique. In this article, a variable-frequency control technique has been utilized to regulate the output voltage. Considering the voltage gain curve of the resonant converter in terms of the normalized angular switching frequency (ω_r), shown in Fig. 9, in order to make sure that the converter operates within the ZVS region, the switching frequency has to be kept above the resonant frequency. Furthermore, as can be seen in Fig. 10, considering the relationship between the overall gain of the converter and ω_r, for the frequencies greater than the resonant frequency, as the switching frequency increases, the gain decreases and vice versa. Therefore, in control system, first, the output voltage of the converter is sensed and is compared with the desired value. Then, the difference (error) is fed into a proportional-integral (PI) controller. The output of the PI controller determines whether the switching frequency has to be increased or reduced to regulate the output voltage. In addition, in order to avoid operating at frequencies below resonance, a limiter is added in the control system to set a lower limit to the operating frequency and to ensure that the converter operates within the ZVS region.

IV. Power Loss Analysis

The total power loss of the proposed dc/dc converter can be divided into SiC switch losses, diode losses, and losses in the resonant circuit.

A. Power Loss Analysis of the SiC MOSFETs

Power losses of an SiC switch mainly consists of steady-state conduction loss, switching loss, and gate charge loss, which are explained as follows.

1) Conduction Loss: The conduction loss of the SiC switches in the proposed converter can be obtained by

$$P_{\rm cond\_loss} = \sum_{n=1}^{6} I_{\rm Si(rms)}^2 R_{\rm on(S_i)} \tag{31}$$

where $R_{{\rm on}(Si)}$ is the switch ON-resistance and the rms current in the switches can be obtained from the resonant current i_p in (4). Since the harmonic components of the resonant current are negligible in loss calculations, i_p can be written as given by

$$i_p = \frac{\sqrt{2}V_i}{\pi\,|Z_i|}\sqrt{(1-\cos 2\pi D)}\sin(\omega_{\rm sw}t + \theta - \varphi_{Z_i}). \tag{32}$$

Consequently the rms current passing through the SiC switches can be obtained as follows:

$$I_{S1} = I_{S6} = \sqrt{\frac{1}{T_s}\int_{t_1}^{t_3}[i_p]^2 dt} = \frac{V_i}{\pi\,|Z_i|}\sqrt{1-\cos(2\pi D)}$$
$$\times\sqrt{D - \frac{t_1}{T_s} + \frac{\sin(2\omega_{\rm sw}t_1 + 2\theta - 2\varphi_{Zi}) - \sin(4\pi D + 2\theta - 2\varphi_{Zi})}{4\pi}}. \tag{33}$$

The maximum rms current passing through the switches can be calculated when t_1 approaches zero ($t1 \to 0$), and consequently, $\varphi Zin \to 0$

$$I_{S1(\max)} = I_{S6(\max)} =$$
$$\frac{V_i}{\pi\,|Z_i|}\sqrt{(1-\cos(2\pi D))\left(D + \frac{\sin(2\theta) - \sin(4\pi D + 2\theta)}{4\pi}\right)}. \tag{34}$$

Similarly, the rms current passing through S_2 and S_5 can be obtained by

$$I_{S2} = I_{S5} = \sqrt{\frac{1}{T_s}\int_{t_5}^{t_7}[i_p]^2 dt} = \frac{V_i}{\pi\,|Z_i|}\sqrt{1-\cos(2\pi D)}$$
$$\times\sqrt{1 - \frac{t_5}{T_s} + \frac{\sin(2\omega_{\rm sw}t_5 + 2\theta - 2\varphi_{Zi}) - \sin(2\omega_{\rm sw}T_s + 2\theta - 2\varphi_{Zi})}{4\pi}}. \tag{35}$$

The maximum current of S_2 and S_5 is given by

$$I_{S2(\max)} = I_{S5(\max)} = \frac{V_i}{\pi |Z_i|} \times \sqrt{(1-\cos(2\pi D))\left(1 - D + \frac{\sin(4\pi D + 2\theta) - \sin(2\theta)}{4\pi}\right)}. \quad (36)$$

2) Switching Loss: According to the waveforms, shown in Fig. 5, the switching losses of the SiC switches can be expressed by

$$P_{\text{sw\_loss}} = \sum_{i=1}^{6}\left[\frac{1}{2}V_S(t_{\text{on}})\cdot I_S(t_{\text{on}})\cdot(t_r + t_{d\_\text{on}})\cdot f_s + \frac{1}{2}V_S(t_{\text{off}})\cdot I_S(t_{\text{off}})\cdot(t_f + t_{d\_\text{off}})\cdot f_s\right] \quad (37)$$

where t_r is the switch rise time, t_f represents the switch fall time, t_{d_on} is the turn-ON delay time, t_{d_off} represents the turn-OFF delay time, and f_s is the switching frequency. Yet considering ZVS turn-ON and ZCS turn-OFF and the fact the *CLLC* resonant converter is utilized to provide soft switching, the switching losses are negligible.

3) Gate Charge Loss: Gate charge loss is the power that dissipates charging the switch gate and can be calculated by (38), where Q_G represents the gate electric charge, C_G is the gate capacitance, and V_G is the gate-source voltage

$$P_{G\_\text{loss}} = \sum_{i=1}^{6} Q_G \cdot V_G \cdot f_s = \sum_{i=1}^{6} C_G \cdot V_G^2 \cdot f_s. \quad (38)$$

B. Power Loss Analysis of the Diodes

The conduction Loss of the diodes is divided into conduction loss and switching loss. Due to the near-zero ZCS turn-ON and turn-OFF of the body diodes of the switches and the added diodes, the switching loss of the diodes can be ignored. As a result, only conduction loss is contributed to the diode loss as

$$P_{G\_\text{loss}} = \sum_{i=1}^{4} R_{Di} \cdot I_{Di\_\text{rms}}^2. \quad (39)$$

where R_{Di} represents the ON-state resistance of the diodes.

C. Power Loss Analysis of the HF Transformer and Inductor

The loss associated with the HF transformer and inductor is divided into conduction loss and core loss. The inductor conduction loss in the secondary side of the resonant circuit can be expressed by (39), where R_{LDC} is the dc resistance of the inductor winding, and $I_{s(\text{rms})}$ represents the rms value of the current in the secondary side of the resonant tank

$$P_{\text{ind\_cond}} = R_{\text{LDC}} \cdot I_{s(\text{rms})}^2. \quad (40)$$

The conduction loss associated with the HF transformer is calculated by (41), where R_{PDC} and R_{SDC} represent the dc resistance of the primary and secondary windings of the HF transformer, respectively

$$P_{\text{TR\_cond}} = R_{\text{PDC}} \cdot I_{p(\text{rms})}^2 + R_{\text{SDC}} \cdot I_{s(\text{rms})}^2. \quad (41)$$

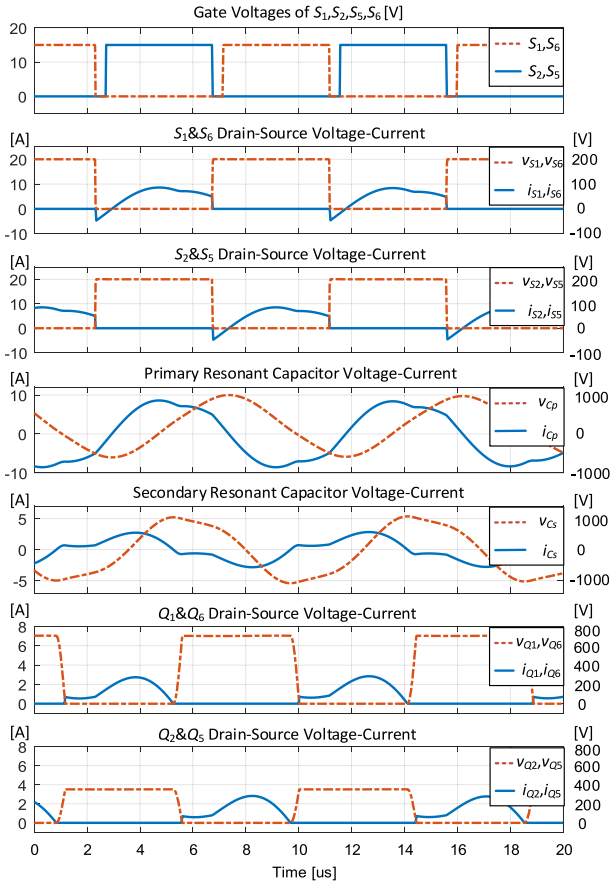

Fig. 13. Simulation waveforms for the boost operating mode.

The core losses of the transformer and the inductor can be obtained by (42), where k_0, α, and β are constants and ΔB is the peak ac flux density expressed by (43), where N represents the number of turns and A_e is the core window area

$$P_{\text{core}} = k_0 \cdot \Delta B^{\alpha} \cdot f_s^{\beta} \quad (42)$$

$$\Delta B = \frac{V_{\text{in}} DT}{4NA_e}. \quad (43)$$

V. Simulation and Experimental Results

The simulation and experimental results are provided in this section to verify the performance of the proposed converter. The simulation waveforms in the boost mode are demonstrated in Fig. 13 for $D = 0.5$. L_M, L_s, C_p, and C_s are 158 μH, 316.07 μH, 16.03 nF, and 6.25 nF, respectively. Fig. 14 compares the output voltage ripple in conventional four-switch converter and the proposed six-switch hybrid converter in boost and buck operating modes, respectively. The switching frequency of the converter is 107 kHz in boost mode. In this mode, S_3 and S_4 are turned ON and Q_3 and Q_4 are turned OFF. As a result the power is delivered to the load for both negative and positive secondary-side resonant current, and hence, the output ripple frequency is increased from 100 to 200 kHz. The simulation results agree with the theoretical analysis.

A 1-kW proof-of-concept prototype, shown in Fig. 15, is designed to verify the operation of the proposed circuit.

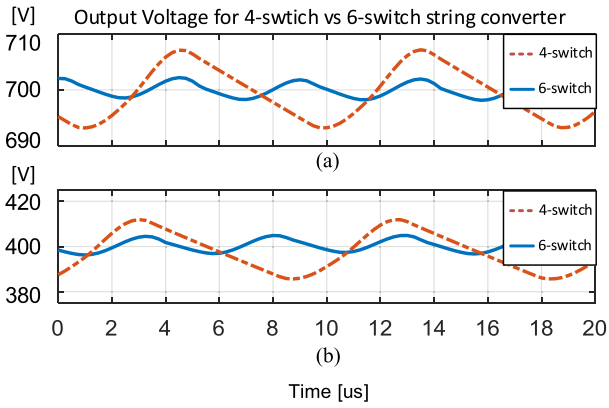

Fig. 14. Output voltage for four-switch versus six-switch string converter in (a) boost operating mode and (b) buck operating mode.

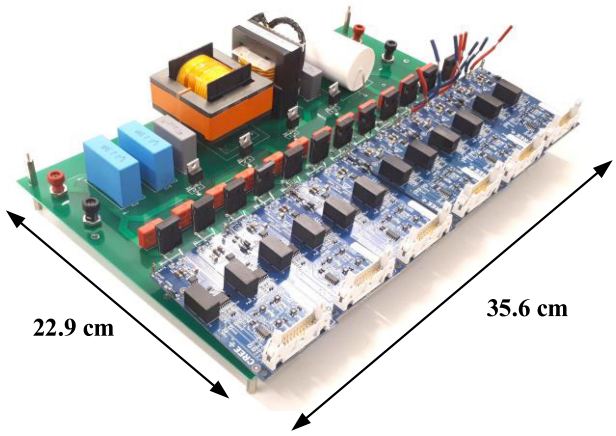

Fig. 15. Proof-of-concept prototype tested in laboratory.

TABLE I
DESIGN SPECIFICATIONS AND CIRCUIT PARAMETERS

Output Power (P_o)	1 kW
Output Voltage (V_o)	700 V
Input Voltage (V_i)	400 V
Magnetizing inductance (L_M)	160 µH
Secondary side resonant inductance (L_s)	320 µH
Primary side resonant capacitance (C_p)	15 nF
Secondary side resonant capacitance (C_s)	5.8 nF
Switching Frequency (f_s)	> 100 kHz
Switches	SiC SCT3080KL
Added Diodes	U1560 Ultrafast Diode
Primary side snubber caps	330 pF
Secondary side snubber caps	150 pF

The component parameters used in the experiments are given in Table I. InfiniiVision MSOX6004A oscilloscope by Keysight Technologies was used to capture the experimental waveforms and measure the provided efficiencies. Fig. 16 demonstrates the voltage and current of the primary and secondary side of the resonant circuit in boost operating mode. Fig. 17 shows the drain–source voltage and current of the inverting side switches. As can be seen, the voltage stress over the switches is half of the dc-link voltage. ZVS turn-ON is provided for all the switches in the inverting block. In the experiment prototype, a snubber

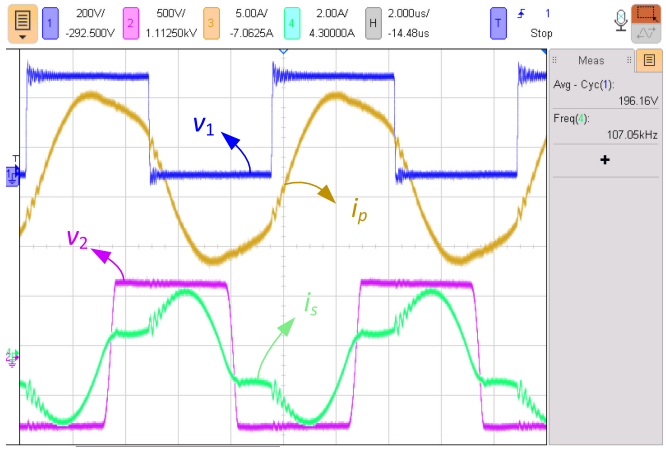

Fig. 16. Experimental waveforms of the converter in boost mode. Voltage and current at the primary and secondary side of the resonant converter.

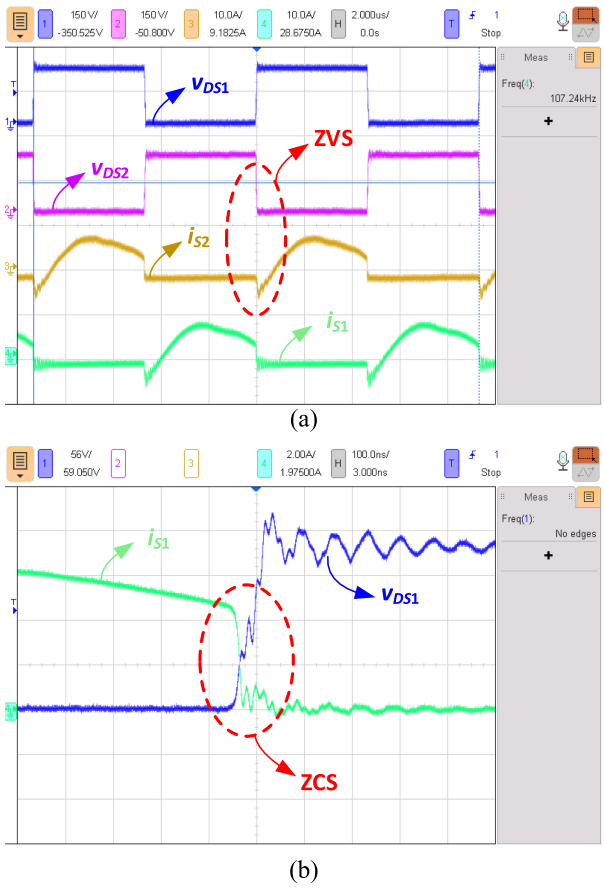

Fig. 17. Experimental waveforms of the converter in boost mode. (a) Drain–source voltage and current of S_1 and S_2 for two switching periods. (b) Zoomed-in snapshot.

capacitor of 330 pF is added across each switch to provide ZCS turn-OFF for the primary-side switches.

The output voltage along with secondary-side resonant current is demonstrated in Fig. 18. The positive current passing through the body diodes of Q_1 and Q_6 is identical to the negative current passing through D_{o1} and D_{o2} and the antiparallel diodes

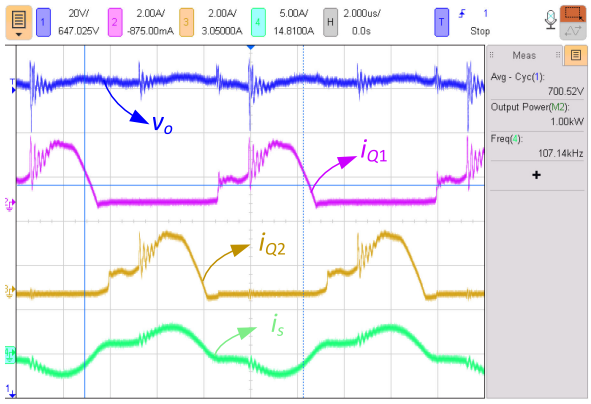

Fig. 18. Experimental waveforms of the converter in boost mode. Converter's output voltage, current of Q_1 and Q_2 in the rectifying block and the current in the secondary side of the resonant circuit.

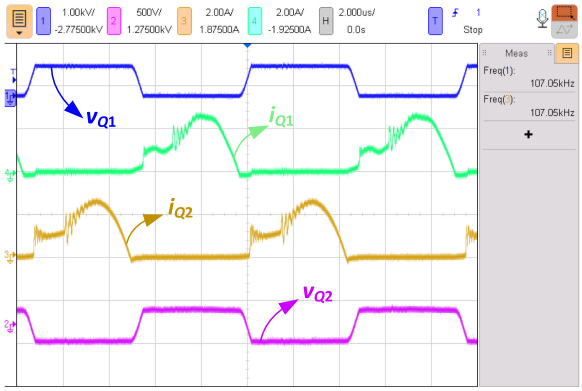

(a)

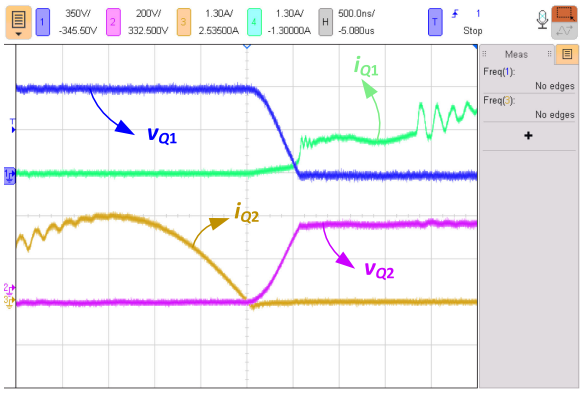

(b)

Fig. 19. Experimental waveforms of the converter in boost mode. (a) Drain–source voltage and current of Q_1 and Q_2 in the rectifying block for two switching periods. (b) Zoomed-in snapshot.

of Q_2 and Q_5. The voltage stress and the current passing through Q_1 and Q_2 are shown in Fig. 19.

Since no gate signals are applied to the rectifying block switches, no switching losses in the rectifying block are associated with the total converter loss in boost operating mode. Fig. 20 shows the voltage stress across the switches and the diodes in the rectifying circuit. Snubber capacitors of 150 pF are utilized

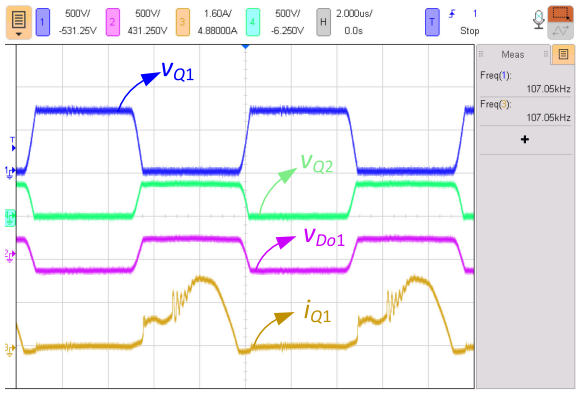

Fig. 20. Voltage stress over Q_1, Q_2, and D_{o1} in the rectifying block and current of Q_1.

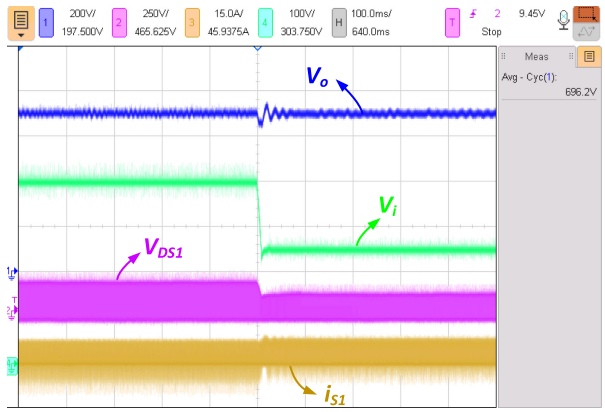

Fig. 21. Dynamic response of the proposed converter for a step input voltage change (400–250 V) with a variable-frequency control technique in the boost mode.

in the secondary side to provide ZCS in the charging mode and to balance the voltage stress over Q_2, Q_5, D_{o1}, and D_{o2}.

In order to evaluate the performance of the control system, two scenarios have been investigated for various loading conditions. In the first scenario, the input voltage has been reduced from 400 to 250 V in the boost mode and it has been investigated whether the converter can regulate the output voltage on 700 V. Dynamic response of the proposed converter for a step input voltage change is shown in Fig 21. As can be seen, the control system has successfully regulated the output voltage to the desired value while providing ZVS for the switches (see Figs. 22 and 23). The zoomed-in snapshots of the experimental waveforms are demonstrated in Figs. 24 and 25. As can be seen, at the time the gate signal is applied to the S_1, the current is passing through its body diode in the opposite direction providing ZVS for S_1.

In the second scenario, the performance of the control system has been investigated in the buck mode. In this mode, the load has been increased from 60% to 100% of the rated power and the performance of the converter in regulating the output voltage has been investigated. As can be seen in Fig. 26, after the load has been increased, the converter has successfully regulated the output voltage in the buck mode by means of the variable-frequency control system while providing ZVS for all of the switches

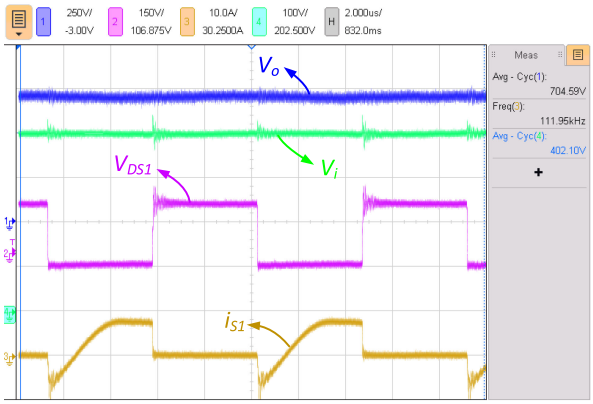

Fig. 22. Experimental waveforms of the converter before the input step change ($V_i = 400$ V) for reduced loading condition.

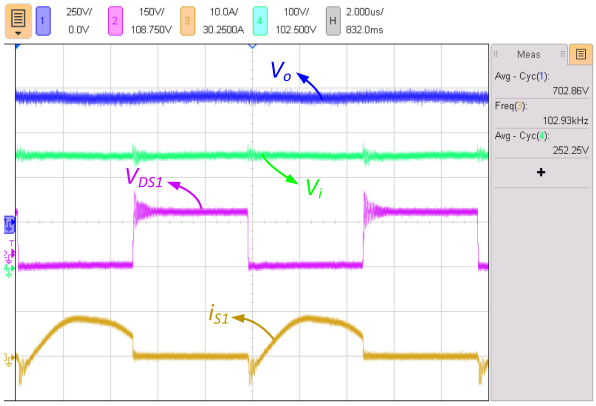

Fig. 23. Experimental waveforms of the converter after the input step change ($V_i = 250$ V) for reduced loading condition.

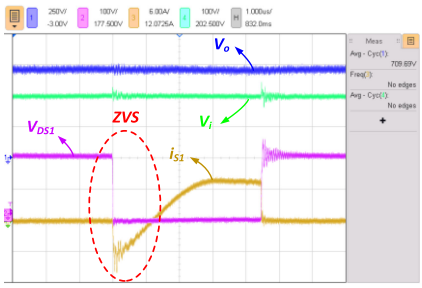

Fig. 24. Zoomed-in snapshot of the experimental waveforms of the converter in boost mode before the input step change ($V_i = 400$ V).

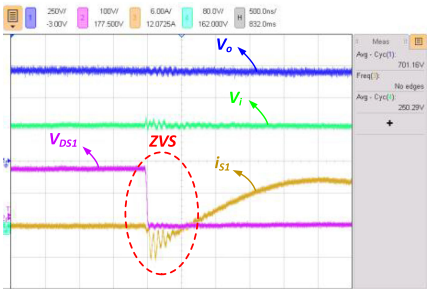

Fig. 25. Zoomed-in snapshot of the experimental waveforms of the converter in boost mode after the input step change ($V_i = 250$).

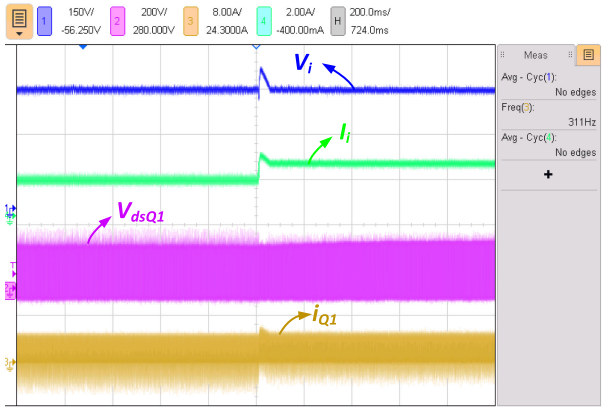

Fig. 26. Dynamic response of the proposed converter for a step load change (from 60% to 100%) with the variable-frequency control technique in buck mode.

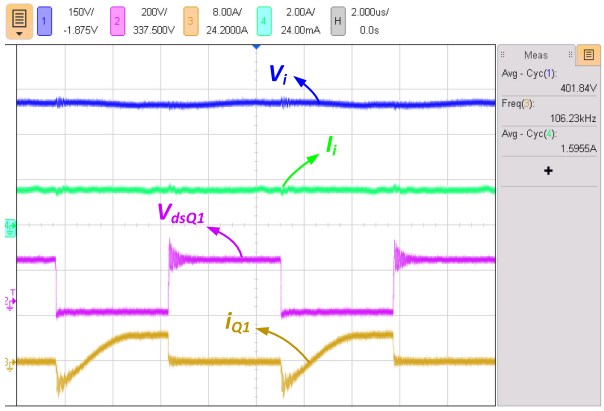

Fig. 27. Experimental waveforms of the converter before the load step change.

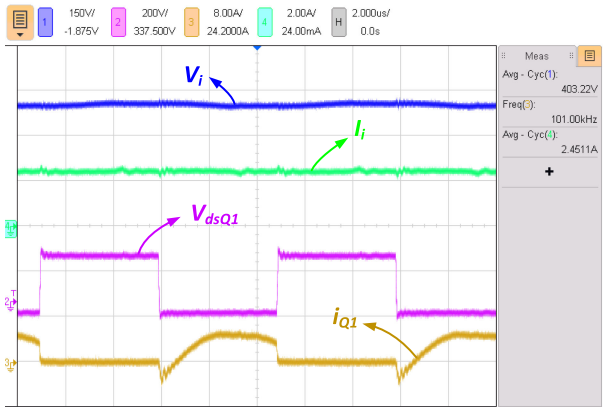

Fig. 28. Experimental waveforms of the converter after the load step change.

(see Figs. 27 and 28). The zoomed-in snapshots of the experimental waveforms are demonstrated in Figs. 29 and 30. Figs. 31 and 32 show the efficiency measurements at the boost and buck mode conditions. Fig. 31 shows the case at the full-load condition at boost mode, where an efficiency of 96.8% is obtained. Fig. 32 shows the efficiency at full load at buck mode.

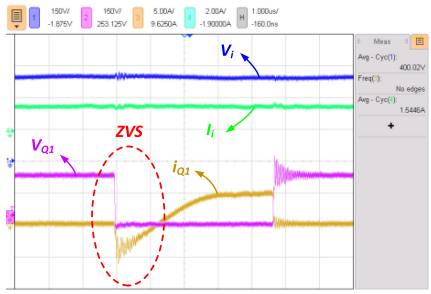

Fig. 29. Zoomed-in snapshot of the experimental waveforms of the converter in buck mode before the load step change.

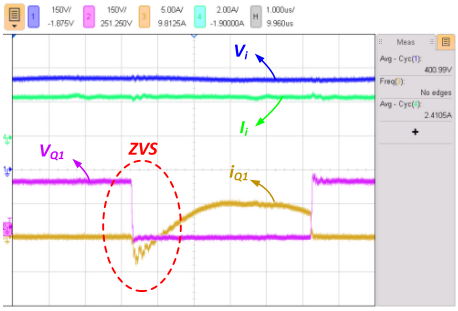

Fig. 30. Zoomed-in snapshot of the experimental waveforms of the converter in buck mode after the load step change.

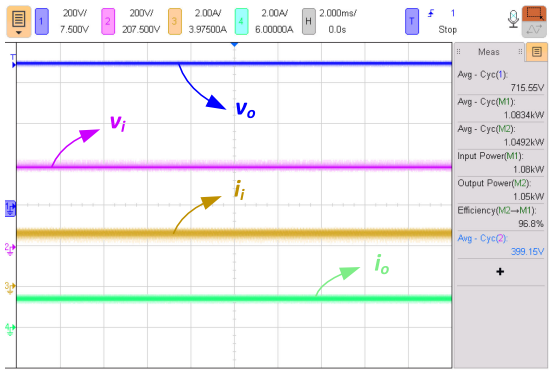

Fig. 31. Experimental waveforms of the converter in boost mode for a 400-V input, 700-V output and a 487-Ω resistive load. Input and output voltages and current waveforms along with the measured efficiency.

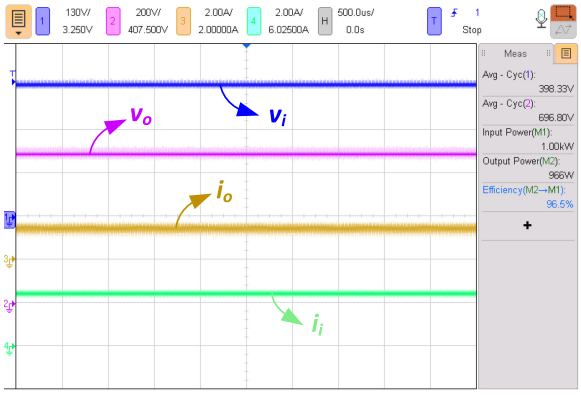

Fig. 32. Experimental waveforms of the converter in buck mode for a 700-V input, 400-V output, and a 160-Ω resistive load. Input and output voltages and current waveforms along with the measured efficiency.

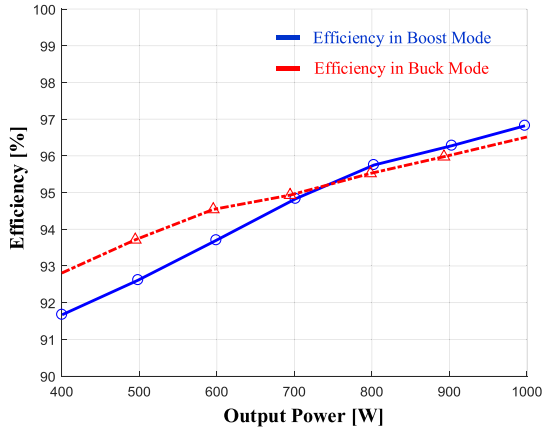

Fig. 33. Efficiency curve of the proposed topology in both charging and discharging modes.

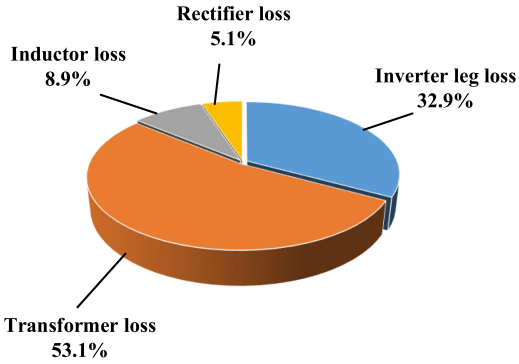

Fig. 34. Loss breakdown of the key components in the prototype.

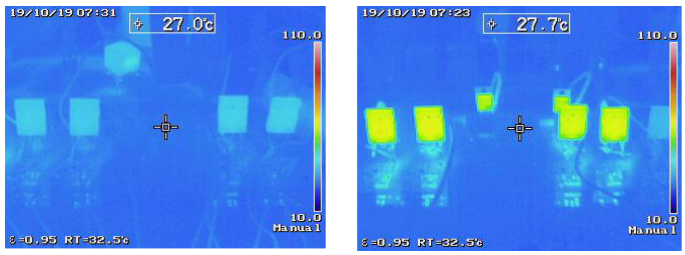

(a) (b)

Fig. 35. Thermal test results of the prototype operating at 1-kW output power in buck mode. (a) Inverting block. (b) Rectifying block.

The efficiency curves of the proposed converter in the boost and buck operating mode are presented in Fig. 33. In order to obtain the efficiency of the total circuit, the input voltage (V_i) and current (i_i) have been connected to the input channels of the oscilloscope and the output voltage (V_o) and current (i_o) have been connected to the output channels and the efficiency analysis option has been selected to calculate the efficiency.

The same approach has been employed to capture the efficiency of the resonant circuit. At 1-kW output power, the designed prototype shows a maximum efficiency of 96.8% in boost mode and 96.5% in buck mode for a switching frequency of 107 kHz. Loss breakdown of the key components in the prototype is shown in Fig. 34. Fig. 35 shows the thermal images

TABLE II
COMPARISON BETWEEN THE EXISTING AND THE PROPOSED BIDIRECTIONAL DC/DC CONVERTER TOPOLOGIES

Topology	Number of semiconductor devices in each leg			Voltage stress over each switch in inverting block	Frequency of the output voltage	Current rating of each switch	Efficiency
	HF switches	LF switches	diodes				
H-bridge	4	-	-	V_{link}	$2\times f_s$	I_o	98% [33]
Three level converter	4	-	2	$\frac{V_{link}}{2}$	$2\times f_s$	I_o	96.5% [26]
4-swtich string circuit	4	-	-	$\frac{V_{link}}{2}$	f_s	I_o	96%
5-swtich string circuit	4	1	2	$\frac{V_{link}}{2}$	$2\times f_s$	I_o	96.8%
The proposed circuit	4	2	2	$\frac{V_{link}}{2}$	$2\times f_s$	I_o	96.8%

of the switches in the inverter and the HF rectifier. It can be observed that the temperature readings are almost the same and are well below the maximum operating temperatures. Compared to the conventional full-bridge-based bidirectional converters, the proposed converter structure reduces the voltage stress of half of the required switches to one-half of either the dc-link voltage or the battery voltage. In addition, the peak-to-peak output voltage ripple in the proposed topology is less than one-half of that in the conventional four-switch string rectifier circuit, allowing much lower output filter capacitance to be used. Table II has been provided to compare the existing and the proposed bidirectional circuit topologies in terms of: semiconductor device count (switches and diodes), efficiency of the converter, voltage and current ratings of the switches, and the diodes and the frequency of the output voltage ripple.

VI. CONCLUSION

A hybrid string inverter/rectifier resonant bidirectional dc/dc converter has been presented in this article for energy storage applications. The employed *CLLC* resonant circuit in the proposed topology allows the circuit to step up/down the voltage levels and to provide soft switching for all the switches and diodes. The operating principles and soft-switching condition of the proposed converter have been analyzed in detail. The design procedures of an example were provided. Simulation and experimental results have been provided on a 1-kW, 700-V output, 100-kHz prototype to highlight the merits of the proposed converter. Dynamic performance and step responses of the proposed converter have been provided. Results confirmed that a peak efficiency of 96.8% in the boost mode and 96.5% in the buck mode were achieved.

REFERENCES

[1] N. R. Averous *et al.*, "Development of a 4 MW Full-Size wind-turbine test bench," *IEEE J. Emerg. Sel. Topics Power Electron.*, vol. 5, no. 2, pp. 600–609, Jun. 2017.

[2] S. Kumar, A. K. Verma, I. Hussain, B. Singh, and C. Jain, "Better control for a solar energy system: Using improved enhanced phase-locked loop-based control under variable solar intensity," *IEEE Ind. Appl. Mag.*, vol. 23, no. 2, pp. 24–36, Mar./Apr. 2017.

[3] M. Yilmaz and P. T. Krein, "Review of battery charger topologies, charging power levels, and infrastructure for plug-in electric and hybrid vehicles," *IEEE Trans. Power Electron*, vol. 28, no. 5, pp. 2151–2169, May 2013.

[4] C. Shi, Y. Tang, and A. Khaligh, "A single-phase integrated onboard battery charger using propulsion system for plug-in electric vehicles," *IEEE Trans. Veh. Technol.*, vol. 66, no. 12, pp. 10899–10910, Dec. 2017.

[5] A. Emadi, Y. J. Lee, and K. Rajashekara, "Power electronics and motor drives in electric, hybrid electric, and plug-in hybrid electric vehicles," *IEEE Trans. Ind. Electron.*, vol. 55, no. 6, pp. 2237–2245, Jun. 2008.

[6] U. K. Madawala and D. J. Thrimawithana, "A bidirectional inductive power interface for electric vehicles in V2G systems," *IEEE Trans. Ind. Electron.*, vol. 58, no. 10, pp. 4789–4796, Oct. 2011.

[7] X. Jia, C. Hu, S. Du, M. Chen, P. Lin, and D. Xu, "DC-link voltage control strategy of a bi-directional DC/DC converter for electric vehicles," in *Proc. IEEE Energy Convers. Congr. Expo.*, 2015, pp. 92–99.

[8] Y. Wang, H. Song, and D. Xu, "Soft-switching bidirectional DC/DC converter with an LCLC resonant circuit," *IEEE J. Emerg. Sel. Topics Power Electron.*, vol. 7, no. 2, pp. 851–864, Jun. 2019.

[9] H.-J. Chiu and L.-W. Lin, "A bidirectional DC-DC converter for fuel cell electric vehicle driving system," *IEEE Trans. Power Electron.*, vol. 21, no. 4, pp. 950–958, Jul. 2006.

[10] B. Lee, J. Kim, S. Kim, and J. Lee, "An isolated/bidirectional PWM resonant converter for V2G(H) EV on-board charger," in *IEEE Trans. Veh. Technol.*, vol. 66, no. 9, pp. 7741–7750, Sep. 2017.

[11] G. Waltrich, M. A. M. Hendrix, and J. L. Duarte, "Three-phase bidirectional DC/DC converter with six inverter legs in parallel for EV applications," *IEEE Trans. Ind. Electron.*, vol. 63, no. 3, pp. 1372–1384, Mar. 2016.

[12] M. Kwon and S. Choi, "An electrolytic capacitorless bidirectional EV charger for V2G and V2H applications," *IEEE Trans. Power Electron.*, vol. 32, no. 9, pp. 6792–6799, Sep. 2017.

[13] D. Das, N. Weise, K. Basu, R. Baranwal, and N. Mohan, "A bidirectional soft-switched DAB-based single-stage three-phase AC–DC converter for V2G application," *IEEE Trans. Transp. Electrific.*, vol. 5, no. 1, pp. 186–199, Mar. 2019.

[14] S. Dusmez, A. Khaligh, and A. Hasanzadeh, "A zero-voltage-transition bidirectional DC/DC converter," *IEEE Trans. Ind. Electron.*, vol. 62, no. 5, pp. 3152–3162, May 2015.

[15] H. S. H. Chung, W.-L. Cheung, and K. S. Tang, "A ZCS bidirectional flyback DC/DC converter," *IEEE Trans. Power Electron.*, vol. 19, no. 6, pp. 1426–1434, Nov. 2004.

[16] B. Zhao, Q. Song, W. Liu, and Y. Sun, "Overview of dual-active-bridge isolated bidirectional DC–DC converter for high-frequency-link power-conversion system," *IEEE Trans. Power Electron.*, vol. 29, no. 8, pp. 4091–4106, Aug. 2014.

[17] J. H. Jung, H. S. Kim, M. H. Ryu, and J. W. Baek, "Design methodology of bidirectional CLLC resonant converter for high frequency isolation of DC distribution systems," *IEEE Trans. Power Electron.*, vol. 28, no. 4, pp. 1741–1755, Apr. 2013.

[18] L. Xue, Z. Shen, D. Boroyevich, P. Mattavelli, and D. Diaz, "Dual active bridge-based battery charger for plug-in hybrid electric vehicle with charging current containing low frequency ripple," *IEEE Trans. Power Electron.*, vol. 30, no. 12, pp. 7299–7307, Dec. 2015.

[19] Y. Liu *et al.*, "V2G bi-directional battery charger with flexible AC/DC converter," in *Proc. IEEE Energy Convers. Congr. Expo.*, 2017, pp. 1439–1445.
[20] P. He, A. Mallik, A. Sankar, and A. Khaligh, "Design of a 1-MHz high-efficiency high-power-density bidirectional GaN-based CLLC converter for electric vehicles," *IEEE Trans. Veh. Technol.*, vol. 68, no. 1, pp. 213–223, Jan. 2019.
[21] S. Jalbrzykowski, A. Bogdan, and T. Citko, "A dual full-bridge resonant class-E bidirectional DC–DC converter," *IEEE Trans. Ind. Electron.*, vol. 58, no. 9, pp. 3879–3883, Sep. 2011.
[22] Z. U. Zahid, Z. M. Dalala, R. Chen, B. Chen, and J. Lai, "Design of bidirectional DC–DC resonant converter for vehicle-to-grid (V2G) applications," *IEEE Trans. Transp. Electrific.*, vol. 1, no. 3, pp. 232–244, Oct. 2015.
[23] J. Park and S. Choi, "Design and control of a bidirectional resonant DC–DC converter for automotive engine/battery hybrid power generators," *IEEE Trans. Power Electron.*, vol. 29, no. 7, pp. 3748–3757, Jul. 2014.
[24] K. Jin, X. Ruan, and F. Liu, "An improved ZVS PWM three-level converter," *IEEE Trans. Power Electron.*, vol. 54, no. 1, pp. 319–329, Feb. 2007.
[25] L. Sih-Yi, J. Jynu-Jhe, L. Jing-Yuan, H. Yao-Ching, and C. Haung-Jen, "High-voltage bi-directional half-bridge three-level series resonant converter with frequency modulation control," in *Proc. Int. Power Electron. Conf./ECCE Asia*, 2018, pp. 645–650.
[26] T. Jiang, J. Zhang, X. Wu, K. Sheng, and Y. Wang, "A bidirectional three-level LLC resonant converter with PWAM control," *IEEE Trans. Power Electron.*, vol. 31, no. 3, pp. 2213–2225, Mar. 2016.
[27] M. Narimani, G. Moschopoulos, and D. Wijeratne, "A comparative study of three-level DC-DC converters," in *Proc. IEEE Energy Convers. Congr. Expo.*, 2013, pp. 3971–3976.
[28] P. Das, M. Pahlevaninezhad, and A. K. Singh, "A novel load adaptive ZVS auxiliary circuit for PWM three-level DC–DC converters," *IEEE Trans. Power Electron.*, vol. 30, no. 4, pp. 2108–2126, Apr. 2015.
[29] P. J. Grbovic, P. Delarue, P. Le Moigne, and P. Bartholomeus, "A bidirectional three-level DC–DC converter for the ultracapacitor applications," *IEEE Trans. Ind. Electron.*, vol. 57, no. 10, pp. 3415–3430, Oct. 2010.
[30] M. Abbasi and J. Lam, "A step-up transformerless, ZV–ZCS high-gain DC/DC converter with output voltage regulation using modular step-up resonant cells for DC grid in wind systems," *IEEE J. Emerg. Sel. Topics Power Electron.*, vol. 5, no. 3, pp. 1102–1121, Sep. 2017.
[31] R. Emamalipour and J. Lam, "A new non-multi-level structured, H-bridgeless DC/DC bidirectional converter with low voltage stress and complete soft-switching operation," in *Proc. IEEE Appl. Power Electron. Conf. Expo.*, 2019, pp. 2322–2328.
[32] M. Bertoluzzo, G. Buja, and G. Pede, "Design considerations for fast AC battery chargers," in *Proc. World Elect. Veh. Symp. Exhib.*, 2013, pp. 1–8.
[33] A. Hillers, D. Christen, and J. Biela, "Design of a highly efficient bidirectional isolated LLC resonant converter," in *Proc. 15th Int. Power Electron. Motion Control Conf.*, Novi Sad, Serbia, 2012, pp. DS2b.13-1–DS2b.13-8.

Reza Emamalipour (Student Member, IEEE) the B.S. degree in power engineering from Shahid Beheshti University, Tehran, Iran, in 2012, and the M.S. degree in power and energy systems from the Department of Electrical and Computer Engineering of the University of Tehran, Tehran, in 2015. He is currently working toward the Ph.D. degree in power electronics with the Advanced Power Electronics Laboratory, Department of Electrical Engineering and Computer Science, Lassonde School of Engineering, York University, Toronto, ON, Canada.

From 2011 to 2017, he was a Research Associate with the Automotive Technology Laboratory, University of Tehran. His research interests include design and control of power electronics converters for renewable energy and energy storage systems, soft-switching bidirectional converters, speed control of electrical machines, and battery management systems.

John Lam (Senior Member, IEEE) received the master's and Ph.D. degrees in electrical engineering from Queen's University, Kingston, ON, Canada, in 2006 and 2010, respectively.

He is currently an Associate Professor with the Department of Electrical Engineering and Computer Science, York University, Toronto, ON, Canada. His research interests include power electronic converters with soft-switching techniques, wide bandgap-based power conversion systems, and renewable energy application.

Dr. Lam was the recipient of the 2018 Outstanding Reviewer Award in the IEEE TRANSACTIONS ON POWER ELECTRONICS. He is an Associate Editor for the IEEE TRANSACTIONS ON POWER ELECTRONICS.